AGU PUBLICATIONS

JGR

Journal of Geophysical Research: Solid Earth

RESEARCH ARTICLE
10.1002/2016JB013179

Key Points:
- 3-D electrical resistivity model obtained by using two-stage inversion of two data types
- Resistivity model shows magmatic variations beneath Kyushu Island
- Electrical resistivity imaging provides insight into the features of arc magmatism

Correspondence to:
M. Hata,
m.hata@aist.go.jp

Citation:
Hata, M., et al. (2017), 3-D electrical resistivity structure based on geomagnetic transfer functions exploring the features of arc magmatism beneath Kyushu, Southwest Japan Arc, *J. Geophys. Res. Solid Earth*, *122*, 172–190, doi:10.1002/2016JB013179.

Received 16 MAY 2016
Accepted 27 DEC 2016
Accepted article online 29 DEC 2016
Published online 17 JAN 2017

3-D electrical resistivity structure based on geomagnetic transfer functions exploring the features of arc magmatism beneath Kyushu, Southwest Japan Arc

Maki Hata[1,2], Makoto Uyeshima[1], Shun Handa[3], Masashi Shimoizumi[4], Yoshikazu Tanaka[5], Takeshi Hashimoto[6], Tsuneomi Kagiyama[5], Hisashi Utada[1], Hiroshi Munekane[7], Masahiro Ichiki[8], and Kiyoshi Fuji-ta[9]

[1]Earthquake Research Institute, University of Tokyo, Tokyo, Japan, [2]National Institute of Advanced Industrial Science and Technology, Tsukuba, Japan, [3]Faculty of Agricultural Science, Saga University, Saga, Japan, [4]Department of Processing Information System Engineering, Kyushu Polytechnic College, Kita-Kyushu, Japan, [5]Aso Volcanological Laboratory, Kyoto University, Chyoyo, Japan, [6]Institute of Seismology and Volcanology, Faculty of Science, Hokkaido University, Sapporo, Japan, [7]Geospatial Information Authority of Japan, Tsukuba, Japan, [8]Research Center for Prediction of Earthquakes and Volcanic Eruptions, Graduate School of Science, Tohoku University, Sendai, Japan, [9]Center for International Affairs, Graduate School of Engineering, Osaka University, Suita, Japan

Abstract Our 3-D electrical resistivity model clearly detects particular subsurface features for magmatism associated with subduction of the Philippine Sea Plate (PSP) in three regions: a southern and a northern volcanic region, and a nonvolcanic region on the island of Kyushu. We apply 3-D inversion analyses for geomagnetic transfer function data of a short-period band, in combination with results of a previous 3-D model that was determined by using Network-Magnetotelluric response function data of a longer-period band as an initial model in the present inversion to improve resolution at shallow depths; specifically, a two-stage inversion is used instead of a joint inversion. In contrast to the previous model, the presented model clearly reveals a conductive block on the back-arc side of Kirishima volcano at shallow depths of ~50 km; the block is associated with hydrothermal fluids and hydrothermal alteration zones related to the formation of epithermal gold deposits. A second feature revealed by the model is another conductive block regarded as upwelling fluids, extending from the upper surface of the PSP in the mantle under Kirishima volcano in the southern volcanic region. Third, a resistive crustal layer, which confines the conductive block in the mantle, is distributed beneath the nonvolcanic region. Fourth, our model reveals a significant resistive block, which extends below the continental Moho at the fore-arc side of the volcanic front and extends into the nonvolcanic region in central Kyushu.

1. Introduction

At the island of Kyushu in the Southwest Japan Arc, the Philippine Sea Plate (PSP) is migrating to the N60°W direction and is subducting beneath the Eurasian plate (Figure 1a). The PSP is classified into three parts: a younger region underlying the Shikoku Basin, an older portion, and a part of the Kyushu-Palau Ridge. Numerous active Quaternary volcanoes along the volcanic front of N30°E–S30°W, related to subduction of the PSP, are present in two separate volcanic regions, one in northern and one in southern Kyushu. Most of those active volcanoes occur in two grabens: the Beppu-Shimabara Graben (BSG) [*Matsumoto*, 1979] in the northern volcanic region and the Kagoshima Graben (KG) [*Hayasaka*, 1987] in the southern volcanic region (Figure 1b). Furthermore, andesitic lava plateaus are widely distributed in the eastern part of the northern volcanic region (in the Hohi volcanic zone) and in the western part of the southern volcanic region (in the Hisatsu, Hokusatsu, and Nansatsu zones) [e.g., *Kamata*, 1989; *Nagao et al.*, 1999], and the Matsuura basalts are distributed on the back-arc side of northern Kyushu [*Matsui et al.*, 1989]. In these zones, numerous epithermal gold deposits occur in late Cenozoic andesitic volcanic rocks related to subduction of the PSP. In the Hohi volcanic zone, those deposits including the Taio gold deposit (the fifth largest in Japan and the third largest on Kyushu) occur along the northern edge of the Beppu-Shimabara graben. The Hisatsu and Hokusatsu zones, in which the Hishikari gold deposit (the largest in Japan) and the Kushikino gold deposit (the fourth largest in Japan and the second largest on Kyushu) occur, are particularly productive. On the other

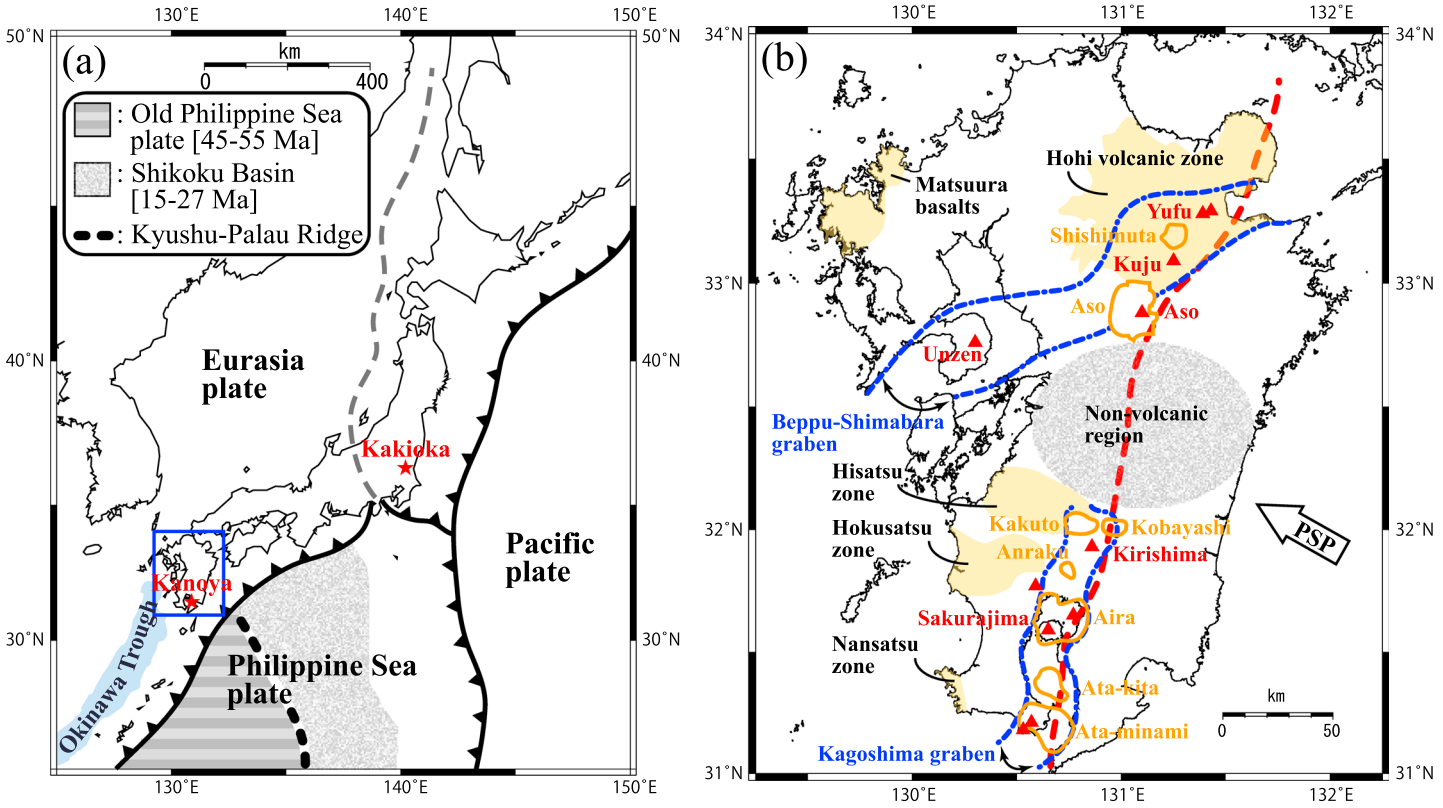

Figure 1. (a) Locations of plate boundaries in the Japan arc (toothed lines). The red stars represent the Kakioka and Kanoya Magnetic Observatories (JMA). A blue box represents the range of Figure 1b. (b) The tectonic setting is characterized by active Quaternary volcanoes (red triangles), calderas (orange rings), two grabens (blue dashed lines), lava plateaus (pale orange shaded regions), and a volcanic front (red dashed line) at Kyushu. The arrow labeled "PSP" indicates the subduction direction of the Philippine Sea Plate. The figure is modified from *Hata et al.* [2015].

hand, no active volcanoes exist in central Kyushu, in the nonvolcanic region (Figure 1). Little is known about the cause of the separation of the active volcanic regions in Kyushu and about the relationship between magmatism (and/or volcanism) and electrical resistivity structures in the mantle wedge beneath Kyushu. To explore these questions in our previous studies, we performed two-dimensional (2-D) and three-dimensional (3-D) inversion analyses to obtain electrical resistivity structures beneath all of Kyushu, using Network-Magnetotelluric (Network-MT) data obtained at 14 periods between 480 and 40,960 s; these data contain geoelectromagnetic information at lithospheric scales [*Hata et al.*, 2012, 2015]. Two major findings of previous studies are described below. First, volcanoes in the northern and southern volcanic regions have different origins, as suggested by two disconnected conductive anomalies in the mantle that are interpreted as two distinct regions of upwelling fluids (aqueous fluids and/or partial melts). Second, the activation of magmatism and the relative contributions of slab-derived fluids to the magmatism vary spatially in all three regions (i.e., in the one nonvolcanic and two volcanic regions).

Previous electrical resistivity models of Kyushu have yielded relatively low-resolution results at shallow depths, on account of sparse Network-MT data in several areas, and the long-period range of the data. Thus, after determining the resistivity structure at greater depths using the Network-MT data, our goal was to obtain an electrical resistivity structure model for shallow depths at a higher resolution and reveal features of arc magmatism in the whole of the Kyushu more precisely than that obtained previously. To achieve this goal, we performed a new 3-D inversion analysis by using a geomagnetic transfer function (TF) calculated on the basis of geomagnetic variation data. Data of geomagnetic variations were obtained for the whole of Kyushu, as well as several small islands in the East China Sea off the western coast of Kyushu. The data were collected from the 1980s to the 2000s [e.g., *Handa*, 2005; *Shimoizumi et al.*, 1997; *Munekane et al.*, 1997; *Fujiwara and Toh*, 1996]. The observation sites are distributed at 10 km intervals over wide parts of Kyushu, as shown in Figure 2a. Moreover, the shortest period of the analysis data is expected to be on the order of several seconds for most of the observation sites. Thus, the density of the geomagnetic variation data is

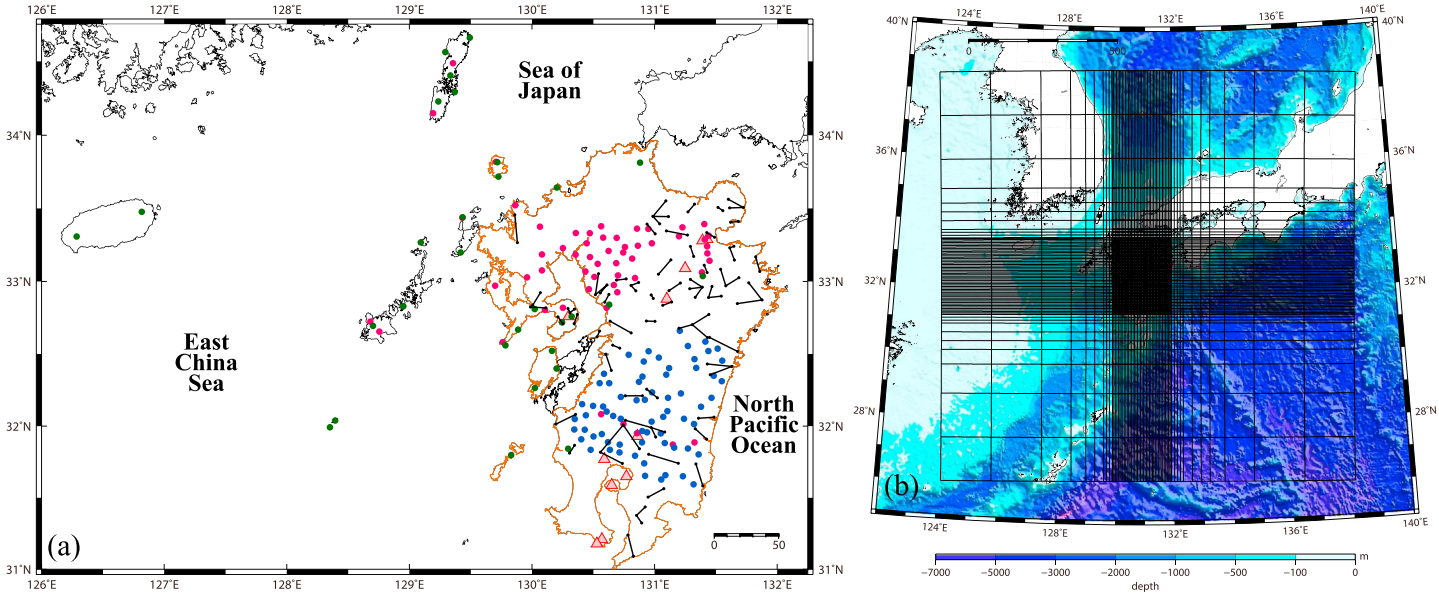

Figure 2. (a) Spatial distribution of geomagnetic observation sites and Network-MT observation sites. The red, blue, and green dots denote the geomagnetic observation sites (see text for details). The black lines with endpoints denote dipoles with two electrodes used to obtain electrical potential difference values. The pink triangles indicate active Quaternary volcanoes. The 136 geomagnetic sites and the 72 Network-MT dipoles, located on Kyushu and the three islands (region outlined in orange), were used in the 3-D inversions. (b) Model space and grid used in the 3-D inversion. The model dimensions are 1400 × 1400 × 1000 km; the grid size was 72 × 60 × 28 cells in the north, east, and vertical (downward) directions, respectively.

considered sufficiently high to derive an electrical resistivity structure model with improved resolution at shallow depths/crustal depth. Besides, geomagnetic TF data are highly sensitive to horizontal variations in an electrical resistivity structure, whereas MT impedance data are also highly sensitive to vertical variations in the structure.

In Japan, observations of geomagnetic variations have been used to investigate subsurface electrical resistivity structures associated with subduction systems since the 1950s [e.g., *Rikitake*, 1969]. For graphical representations of geomagnetic variations, induction vector analysis [*Parkinson*, 1962] is widely used, as the induction vector (arrow) points to an electric current concentration associated with a conductive anomaly. Induction arrows on Japanese arcs generally point to the Pacific Ocean of deep sea in a large sense [e.g., *Yukutake et al.*, 1983]. However, induction arrows in northern and central Kyushu point to the relatively shallow East China Sea [e.g., *Handa et al.*, 1992], rather than to the Pacific Ocean. In southern Kyushu, induction arrows derived from short-period (less than several hundred seconds) data on the western and eastern coasts point to the East China Sea and the Pacific Ocean, respectively, whereas arrows of long-period (greater than several hundred seconds) data are oriented parallel to the coastline [e.g., *Shimoizumi et al.*, 1997; *Munekane*, 2000]. The complex behavior of the induction arrows observed on Kyushu is considered to result from the properties of subsurface electrical resistivity structures. Moreover, a highly conductive layer in the upper mantle (depth, 50–100 km) has been found beneath the East China Sea, as inferred from geomagnetic variation data [e.g., *Handa et al.*, 1992; *Shimoizumi et al.*, 1997]. *Toh and Honma* [2008] also presented evidence for large-scale mantle upwelling centered in the East China Sea, based on large anomalies determined by using thin sheet modeling with geomagnetic variation data. However, the complex behavior of the observed induction arrows cannot be well expressed by models derived from the thin sheet models or the two-dimensional inversion models [e.g., *Shimoizumi et al.*, 1997; *Handa*, 2005; *Toh and Honma*, 2008], although the behavior of the observed arrows suggests the presence of highly conductive anomalies beneath the East China Sea.

In this study, we generated a 3-D electrical resistivity structure model by inverting available geomagnetic TF data, obtained on Kyushu and three small islands (as shown in Figure 2a), by using a 3-D inversion code [*Siripunvaraporn and Egbert*, 2009]. A previous 3-D model [*Hata et al.*, 2015], which was based on inverted Network-MT data (black lines with two dots in Figure 2a) by using another 3-D inversion code

[*Siripunvaraporn et al*., 2004], is used as the starting model for the 3-D inverse modeling in this study. Our new 3-D model, for which the synthetic induction arrows are consistent with observed arrows, provides a higher-resolution model than the previous model [*Hata et al*., 2015], especially at shallow depths.

2. Data Processing

2.1. Geomagnetic Variation Data

In this study, geomagnetic TF data were introduced to improve the resolution at crustal depths of an electrical resistivity structure model obtained previously by using only Network-MT data [*Hata et al*., 2015]. Observed three-component geomagnetic variations are converted to TFs, expressed as $Hz(\mathbf{r}, T) = Ax(\mathbf{r}, T)\, Hx(\mathbf{r}, T) + By(\mathbf{r}, T)\, Hy(\mathbf{r}, T)$, where $Hz(\mathbf{r}, T)$ is the vertical geomagnetic field, $Hx(\mathbf{r}, T)$ and $Hy(\mathbf{r}, T)$ are the horizontal components of the geomagnetic field, $\mathbf{r}$ is the location of observation sites, and T is the period. The geomagnetic TFs $Ax(\mathbf{r}, T)$ and $By(\mathbf{r}, T)$ are complex values. The electrical resistivity structure is determined by using the two TFs of $Ax(\mathbf{r}, T)$ and $By(\mathbf{r}, T)$, which are sensitive to the distribution of the gradient of electrical conductivity (1/resistivity) [e.g., *Rikitake and Yokoyama*, 1953].

Three components of the geomagnetic variation data had been recorded digitally at 1 s intervals at a resolution of 0.001 nT for 1 day and at 10 s or 60 s intervals at a resolution of 0.01 nT for 1 month at the longest, using three types of fluxgate magnetometer systems (U30, U36, and U43; manufactured by TIERRA TECNICA Ltd.); the data had been obtained from the 1980s to the 2000s [e.g., *Handa*, 2005; *Shimoizumi et al*., 1997; *Munekane et al*., 1997]. We collected available data sets among those data for this study. A data set was geomagnetic TFs of $Ax(\mathbf{r}, T)$ and $By(\mathbf{r}, T)$, which had been determined well already, for 67 observation sites in the southern part of Kyushu (blue dots in Figure 2a). The other data set was geomagnetic variation data of $Hx(\mathbf{r}, T)$, $Hy(\mathbf{r}, T)$, and $Hz(\mathbf{r}, T)$, which was re-analyzed to obtain its geomagnetic TF as described in the next paragraph, for 100 observation sites in the northern part of Kyushu and on nearby islands (red and green dots in Figure 2a).

The geomagnetic TFs for the 67 sites (blue dots in Figure 2a) in southern Kyushu had been determined with high signal-to-noise (S/N) ratios for 32 periods, in the range of 4.6–1000 s, using the Robust Remote-Reference MagnetoTelluric (RRRMT) data processing code [*Chave et al*., 1987; *Chave and Thomson*, 1989]. On the other hand, since old TFs had been determined without the use of a remote-reference procedure, we newly determined geomagnetic TFs for the 100 sites (red and green dots in Figure 2a) in northern Kyushu by using the Bounded Influence Remote-Reference magnetotelluric data-Processing (BIRRP) code [*Chave and Thomson*, 2004]. Moreover, before the remote-reference procedure, we eliminated the ionospheric and oceanic tidal components from the long-period (60 s interval) data using a detide code [*Fujii*, 2004], as the tidal components especially affect long-period data and result in distortion of the estimated electrical resistivity structure [*Egbert et al*., 1992]. The magnetic data recorded at the Kakioka Geomagnetic Observatory (KAK) of the Japanese Meteorological Agency (JMA) (shown in Figure 1) were used as a remote reference site for all of the TFs in southern and northern Kyushu. In addition, magnetic data at 1 s intervals were averaged and resampled at 10 s or 60 s intervals, depending on the sampling interval of the original geomagnetic data at each observation site. Geomagnetic TFs for 31 of the 100 sites in northern Kyushu (green dots in Figure 2a) were determined for 22 periods, in the range of 5–7680 s (for 1 s interval data), and for 18 periods in the range of 160–61,440 s (for 60 s interval data), in accordance with data durations. The TFs for the other 69 sites (red dots in Figure 2a) were also determined for 14 periods in the range of 5–480 s (for 1 s interval data), for 16 periods in the range 20–3840 s (for 10 s interval data), and for 10 periods in the range 160–3840 s (for 60 s interval data), after a time-correction process. We adjusted the analyzing periods for the respective sites to obtain TFs of the same periods at the data processing, so that those periods can be partially overlapped with each other.

To obtain the 3-D electrical resistivity structure beneath the whole of Kyushu using 3-D inverse modeling, we utilized data from 136 sites: 67 sites in southern Kyushu (blue dots), 53 sites in northern Kyushu (red dots), and 16 sites in northern Kyushu or the three islands (green dots), as shown in Figure 2a (orange outline islands). We omitted data from the remaining 31 sites, located on islands that are distant from Kyushu Island, because of the difficulty in sufficiently discretizing the coastlines of the islands and the bathymetry at the cell sizes used in the 3-D modeling (shown in Figure 2b). Moreover, the 3-D inversion code requires that only one site exists in each cell.

2.2. Network-MT Data

The Network-MT measurements and the data processing required to prepare the starting model for the present 3-D inverse modeling are briefly described below. The Network-MT response functions $Rx(\mathbf{r}, T)$ and $Ry(\mathbf{r}, T)$ were determined between the electrical potential difference $V(\mathbf{r}, T)$, recorded at each dipole, and the horizontal components of the geomagnetic field, $Hx(\mathbf{r}, T)$ and $Hy(\mathbf{r}, T)$, recorded at a magnetic observatory, where $\mathbf{r}$ and T denote the locations of observation sites and the period. The Network-MT Response Functions (RFs) are defined as $V(\mathbf{r}, T) = Rx(\mathbf{r}, T)\, Hx(\mathbf{r}, T) + Ry(\mathbf{r}, T)\, Hy(\mathbf{r}, T)$. The electrical resistivity structure was determined by using the two complex RFs for each dipole. In the Network-MT measurements, metallic wires leased from a telephone company were used to measure the electrical potential difference. Dipole lengths were approximately 10–30 km on Kyushu (black lines with endpoints in Figure 2a). The advantage of the Network-MT method, as compared with the conventional MT method, is that data can be obtained with high S/N ratios and without static shift effects because the potential differences are measured by using long dipoles. Further theoretical details of the Network-MT method and analysis are described by *Uyeshima* [2007]; details of the Network-MT observations on Kyushu and the processing procedure for the Network-MT RFs are described by *Hata et al*. [2012, 2015]. In our previous 3-D inverse modeling, the RFs for 72 dipoles with high S/N ratios (Figure 2a) were determined for 14 periods in the range of 480–40,960 s, using the RRRMT data processing code [*Chave et al*., 1987; *Chave and Thomson*, 1989].

3. 3-D Electrical Resistivity Imaging Using Geomagnetic TFs

The goal of the 3-D inversion was to obtain a high-resolution model, especially at shallow depths, by using 136 geomagnetic TFs for 12 periods between 20 s and 960 s; the resolution is higher than that obtained by previous electrical resistivity models solely based on Network-MT data for 14 periods between 480 and 40,960 s. The inverted data size ($136 \times 4 \times 12$) was based on the two complex TFs of the 136 sites for 12 periods. Figure 2b shows the model space dimension of $1400 \times 1400 \times 1000$ km; this size was selected to avoid the effects of outer boundaries of the model space on the synthetic data. The model space consisted of $72 \times 60 \times 28$ cells (model parameter size M) in the north (X), east (Y), and vertical (Z) directions, respectively. The smallest cell size in the X and Y directions was 5×5 km, with the size increasing outward. In the Z direction, the cell sizes gradually increased from 10 m in the first surface layer to 500 km in the lowermost layer (vertically variable grid spacing of 0.01, 0.03, 0.06, 0.1, 0.3, 0.5, 1, 3, 5×11, 10×4, 50×2, 100, 200, and 500 km through the model).

We performed the 3-D inversion by using the parallelized "WSINV3DMT" of an Occam's style 3-D inversion code [*Siripunvaraporn and Egbert*, 2009], which applies a data-space method to reduce the computation time. In the 3-D inversion code, three input models (a starting model, a prior model ($\mathbf{m}_0$), and a control model) are given, and an optimum model ($\mathbf{m}$) is iteratively determined by using the constraint that $\mathbf{m} - \mathbf{m}_0$ is spatially smooth. The model fit to observations is evaluated by using the root-mean-square (RMS) misfit, $\mathrm{RMS} = \sqrt{\sum_{i=1}^{N} C_{di}^{-2} \left(d_i - F[m]_i\right)^2 / N}$, where d is the observed data, $F[m]$ is the synthetic data (the forward response of an optimum model ($\mathbf{m}$)), C_d is the error of the data (the data covariance), and N is the parameter size ($136 \times 4 \times 12$, as described above). The prior model is used to constrain the solution to fit a priori information during the inversion, whereas the control model is used to fix values of known features, such as seawater by specifying the bathymetry. The series of iterations in an inversion continues until the maximum iteration number is reached (10 iterations in this study). Alternatively, the iterations are terminated when the RMS misfit reaches a target value or desired level (1.0 ± 0.05 in this study).

For this 3-D inversion, we used the 3-D resistivity model, which was obtained previously by using only Network-MT data [*Hata et al*., 2015], as a starting model and a prior model in the regularization calculation. Thus, the Network-MT data were only used to obtain the starting model and the prior model in this study. In all the models, the resistivity of seawater blocks was fixed at 0.33 Ωm. Then, the following three-step procedure was used to invert the TFs data of the 136 sites, because we consider that a multistep procedure leads to a more reliable and rapid convergence than a single-step procedure for mitigating the local minimum problem in an unconstrained function; i.e., by expanding the acceptable search space (setting a relative error floor to a large value) at the first step and narrowing the search space (setting a relative error floor to a smaller value) at the last step. The unconstrained function is defined as

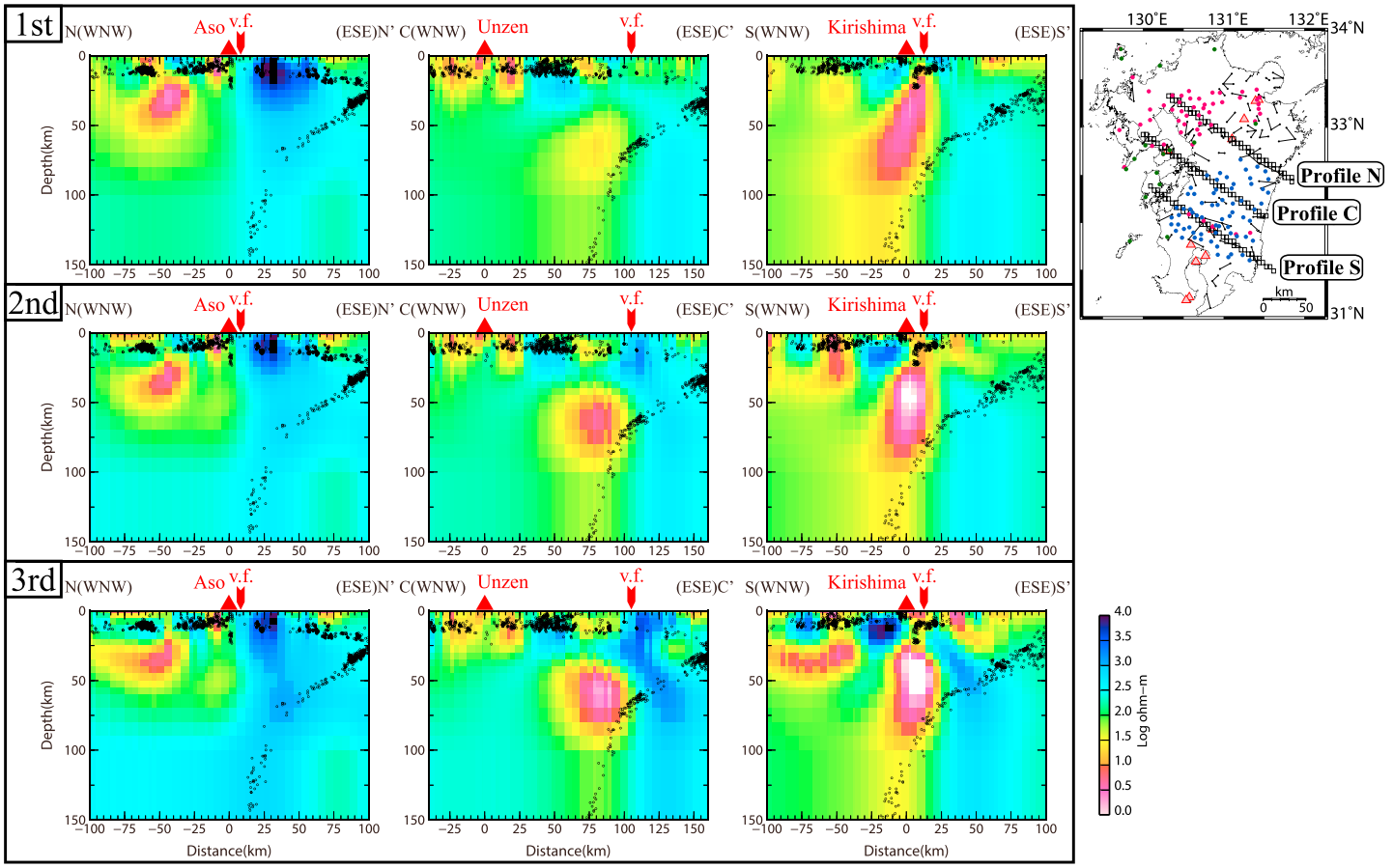

Figure 3. Cross sections of the 3-D resistivity models generated by the three-step procedure along the three profiles shown in the inset map (top right). Results of the previous 3-D resistivity model [*Hata et al*., 2015] were used in the first inversion in the initial model. The map shows positions of the three profiles in meshes, the 136 geomagnetic observation sites (red, blue, and green dots), the 72 Network-MT dipoles (black lines with endpoints), and active volcanoes (red triangles). The three cross-sections rows, from one to three, show the 3-D model after the first, second, and third inversions, respectively. The black dots on the cross sections are the hypocenters of earthquakes within 10 km of each profile, as determined by the JMA from June 2002 to May 2006. The red triangles represent volcanoes (N–N′: Aso, C–C′: Unzen, and S–S′: Kirishima). The red arrows labeled "v.f." represent the position of the volcanic front.

$$U(\mathbf{m},\quad \lambda) = \lambda^{-1}\left\{(\mathbf{d}-\mathbf{F}[\mathbf{m}])^{T}\mathbf{C_d}^{-1}(\mathbf{d}-\mathbf{F}[\mathbf{m}]) - \chi^{2}\right\} + (\mathbf{m}-\mathbf{m}_0)^{T}\mathbf{C_m}^{-1}(\mathbf{m}-\mathbf{m}_0),$$

where λ^{-1} is a Lagrange multiplier, χ^2 is the desired level of RMS misfit, $\mathbf{C_m}$ is the model covariance matrix, and the superscript T represents the transpose. A model whose RMS misfit is closest to 1.0 is always selected as the final model in each inversion step. The final model in the previous inversion step is used as the initial model in the next inversion step. An error floor in the three steps is set to 30% for the first step, 15% for the second step, and 10% for the third step for all TFs [*Ax*(**r**, *T*) and *By*(**r**, *T*)].

Figure 3 shows three cross sections along profiles N (north), C (central), and S (south) for each final model in the three-step procedure. The RMS misfit of each final model is 0.9721 for the first step, 0.9709 for the second step, and 0.9981 for the third step. Structures in the three 3-D electrical resistivity models appear roughly similar, although the structure in the third inversion step shows the highest contrast between marked conductive and resistive blocks. Such features of the resistivity structure models were also indicated by *Hata et al*. [2015]. We thus obtained the 3-D resistivity model which gives a good matching with the observed geomagnetic TFs at the third inversion step. Fits between observed and synthetic data, which gradually improve at every step, can be found by using sounding curves of the geomagnetic TFs [*Ax*(**r**, *T*) and *By*(**r**, *T*)] for three representative observation sites along three profiles, as shown in Figure 4.

Figure 5 shows geomagnetic TFs [*Ax*(**r**, *T*) and *By*(**r**, *T*)], as expressed by induction arrows, at periods of 40, 160, 480, and 960 s for the observed data (gray arrows) and synthetic data of the final model at the third inversion

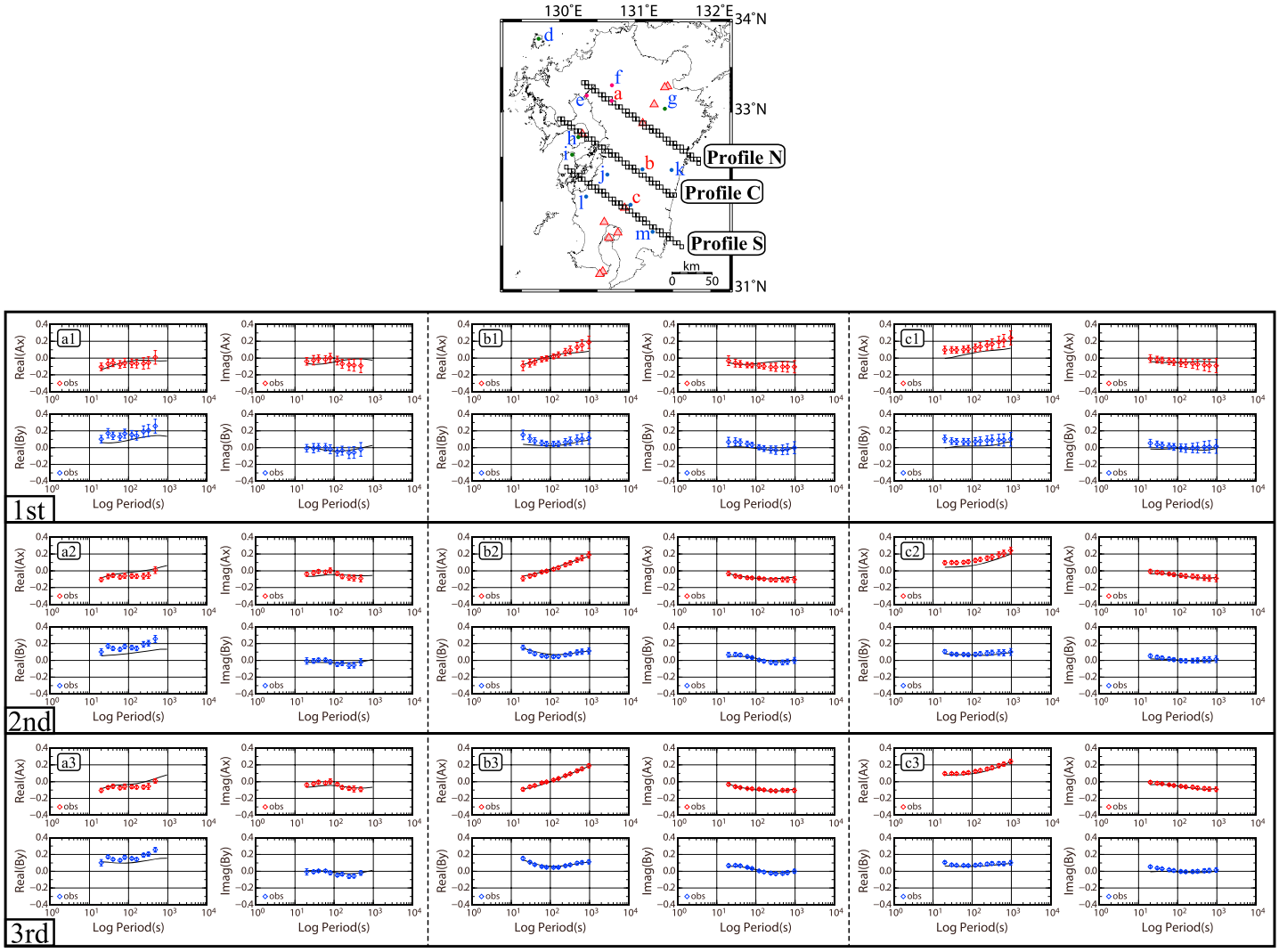

Figure 4. Sounding curves of the geomagnetic transfer functions (*Ax* and *By*) for three observation sites shown in the map as one red and two blue dots designated by the red letters a, b, and c. The black lines and open diamonds with error bars, whose lengths depend on respective error floors in the three-step inversions, indicate synthetic and observed data, respectively. The sounding curves on rows one to three show the 3-D model after the first, second, and third inversions, respectively.

step (color arrows). A pair of real and imaginary induction arrows are defined by two complex numbers ($-Ax$, $-By$) of the respective geomagnetic TFs. The lengths and directions of real arrows are used as an indicator of conductive anomalies, as the arrows tend to point toward conductive anomalies and become longer as the conductivity contrast increases. Figure 6 shows fits between observed and synthetic data of the geomagnetic TFs, as represented by sounding curves, for 10 representative observation sites, as shown on the map in Figure 4. The 10 sites and the 3 sites mentioned previously, which were selected from among the 136 observation sites, are distributed evenly over the entire ground surface in the study area. The synthetic induction arrows of both the real and imaginary parts (colored arrows in Figure 5) are consistent with the observed induction arrows (gray arrows in Figure 5) in magnitude at nearly all sites and all periods. On the other hand, the directions of the observed and synthetic arrows are not in agreement in two regions: the east coast of southern Kyushu and the western side of northern Kyushu. On the east coast of southern Kyushu, the synthetic induction arrows of the real part must be directed more southward for long periods. On the western side of northern Kyushu, the synthetic arrows of the real and imaginary parts remain a dispersion for all periods. By comparing the sounding curves of the observed and synthetic geomagnetic TFs (Figure 6), the respective causes for the misfits on southern Kyushu and northern Kyushu are attributable to a lack of strict model fit for the former, and variations in the observed data for the latter. Besides, the cell sizes of the model,

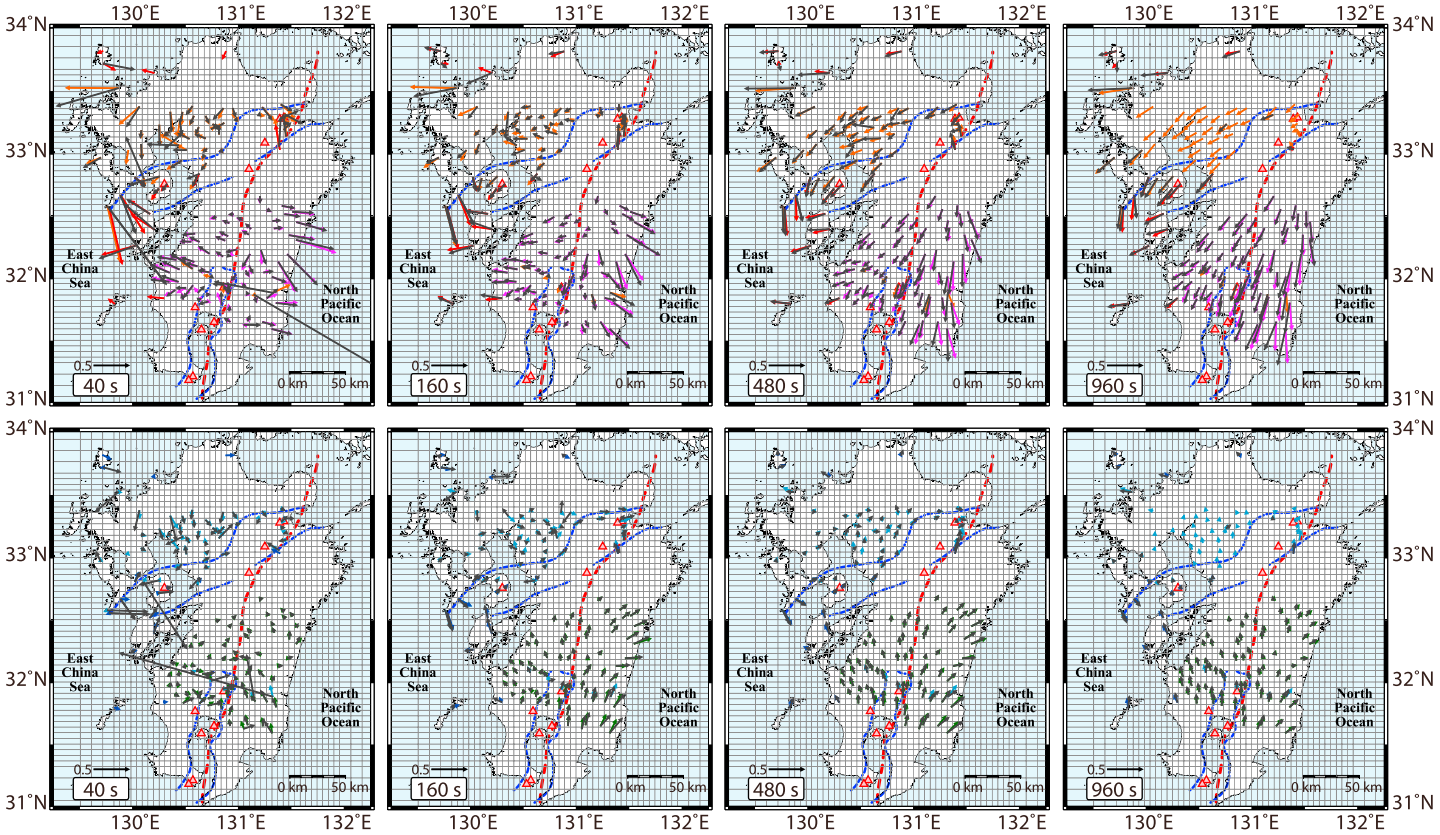

Figure 5. Observed induction arrows (gray arrows) and synthetic induction arrows (colored arrows) for the final model determined by the geomagnetic TFs through the three-step inversion procedure at periods of 40, 160, 480, and 640 s. Warm colors in the upper maps and cool colors in the lower maps indicate real and imaginary parts of the geomagnetic TFs, respectively. The red triangles, blue dashed lines, and a red dashed line represent active volcanoes, two grabens, and a volcanic front.

which are too coarse to accurately represent the coastlines and the distribution of surrounding seawater, are another likely cause of high misfit for sites located near to the coast. We conclude that the final 3-D model is capable of representing the subsurface structure at shallow depths because even the trend of the synthetic geomagnetic TFs at the sites in the two regions conforms to the trends of the observed TFs.

The main features of the real induction arrows (as shown in Figure 5) are as follows. At periods of 40 s and 160 s, real induction arrows locally point toward Yufu and Kirishima volcanoes, at the northwestern edge of the BSG, and at a submarine portion of the southwestern extension of the BSG (see Figure 1b). Thus, conductive crustal blocks are likely to occur beneath these areas. On the other hand, the general trend of the induction arrows for the two periods changes drastically along the boundary of the volcanic front of N30°E–S30°W. The induction arrows on the west coast point toward the East China Sea, whereas those on the east coast point toward the Pacific Ocean. At periods of 480 s and 960 s, induction arrows in southern Kyushu are parallel to the coastline. In addition, induction arrows in northern Kyushu point toward a location in the East China Sea, although the observational data for long periods are missing in northern Kyushu (as mentioned earlier), and thus, only the synthetic arrows are shown on maps for 960 s in Figure 5. Several of these features have already been discussed in previous studies [*Handa et al.*, 1992; *Shimoizumi et al.*, 1997; *Munekane*, 2000].

We used two computing platforms for the inversion procedure. The first was an Intel Xeon system (CPU X7542, operating at 2.66 GHz; a system of the Earthquake Information Center of the Earthquake Research Institute, University of Tokyo), which allowed the use of 48 processors per single inversion; a CPU time limit of 70 h was imposed. We used the system for inverting the 136 geomagnetic TFs, because the inversions finished within the CPU time limit. The run time per iteration was 10+ h in real time (7+ h in CPU time). The other platform was an Intel Xeon with 24 processors (CPU X5690, operating at 3.47 GHz), which was used for sensitivity tests based on the actual measurement configuration of the Network-MT data.

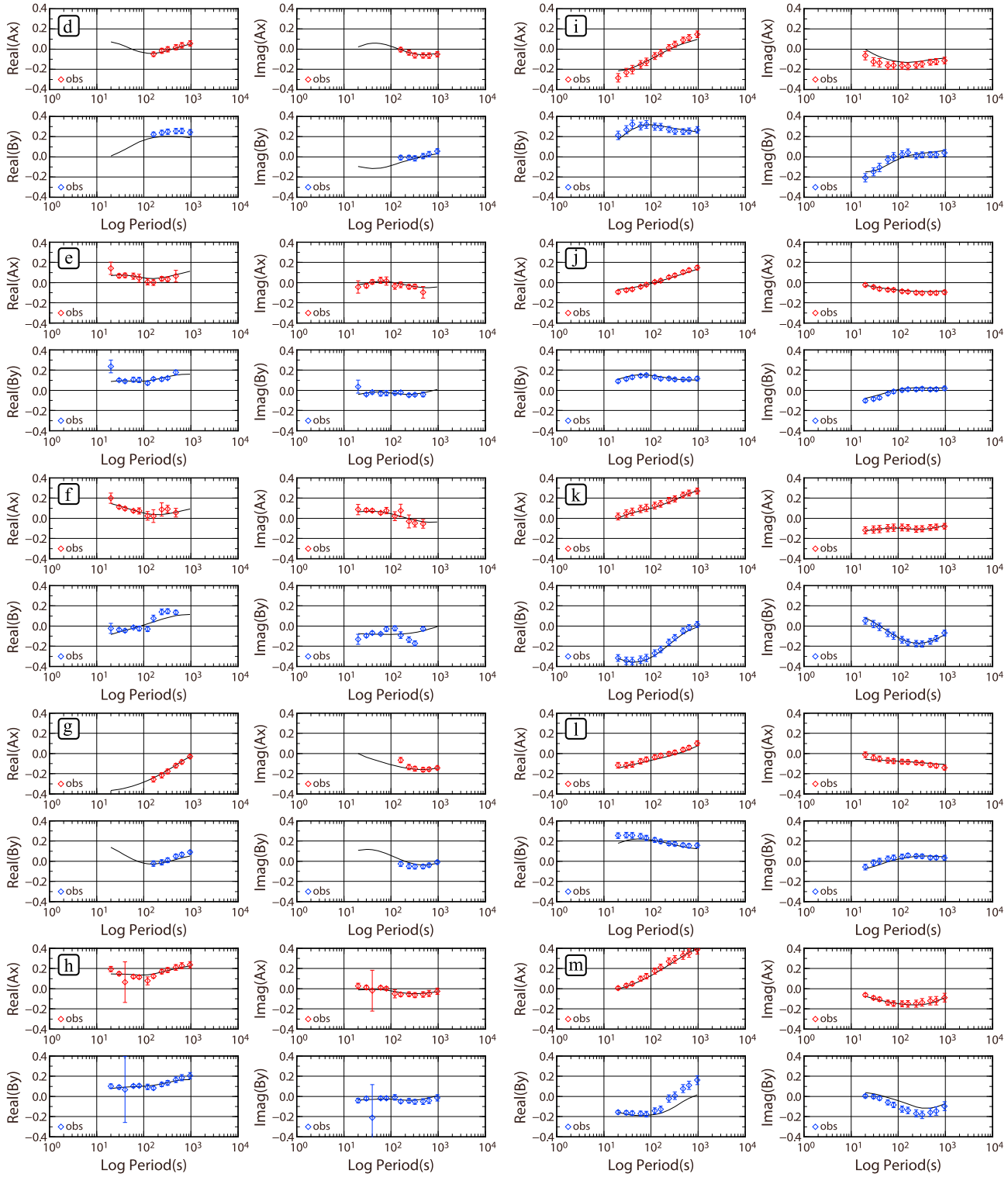

Figure 6. Sounding curves of the geomagnetic transfer functions (*Ax* and *By*) at 10 representative observation sites, shown on the map in Figure 4 as colored dots with blue letters (d–m). The black lines and open diamonds with error bars indicate synthetic data of the final model and observed data, respectively.

4. Sensitivity Tests for Comparative Verification of Model Resolutions

The goal of this study was to obtain a 3-D electrical resistivity model at shallow depths with a resolution higher than that of previous 2-D and 3-D models, which were obtained solely by the Network-MT RFs, by introducing geomagnetic TFs. We performed sensitivity tests to compare respective model resolutions by using actual measurement configurations (such as the spatial distribution of observation sites and sets of data periods) for the geomagnetic and the Network-MT data. Eight inversions were performed by using synthetic data, to which a 5% Gaussian noise was added to estimate the model resolution; this was accomplished by using four checkerboard patterns in Figures 7a–7d (also see in Figure A1). Four of the eight inversions (Figures 7a′–7d′) were performed by using the geomagnetic data configuration, whereas the other four inversions (Figures 7a″–7d″) were performed using the Network-MT data configuration. Conductive and resistive values of all checkerboard blocks were set at 3 and 3000 Ωm, respectively. In all eight inversions, the initial model consisted of an 80 Ωm uniform Earth and 0.33 Ωm seawater, except for layers/blocks in areas of the checkerboard patterns. The 80 Ωm uniform Earth was selected based on RMS misfits for three initial models (the given electrical resistivity structure) of an 80, 200, and 500 Ωm uniform Earth, because the 80 Ωm uniform Earth shows a minimum value among the three initial models. The checkerboard patterns have the same dimensions in the *X* and *Y* directions (250 × 200 km) and were classified into two patterns according to the sizes of the conductive and resistive blocks. In addition, the conductive and resistive blocks are interchangeable between Figures 7a and 7b and 7c and 7d). Figures 7a and 7b show the checkerboard patterns composed of 80 blocks (25 × 25 km alternating in the horizontal direction) for shallow depths, whereas Figures 7c and 7d show the patterns composed of 20 blocks (50 × 50 km alternating in the horizontal direction) at deeper depths. Each depth range (thickness in the *Z* direction) of the checkerboard patterns is 0–10 km (Figures 7a and 7b) or 10–40 km (Figures 7c and 7d).

The final RMS misfits of the eight checkerboard test models are 0.9758 for Figure 7a′, 0.9676 for Figure 7b′, 1.0229 for Figure 7c′, 1.0011 for Figure 7d′, 0.9573 for Figure 7a″, 0.9817 for Figure 7b″, 1.0149 for Figure 7c″, and 1.0175 for Figure 7d″, with the relative error floor set to 10% for all geomagnetic TFs and to 5% for all Network-MT RFs. We applied the same multistep procedures that were used to obtain the respective final models, as mentioned in section 3 and in *Hata et al*. [2015], to the eight checkerboard test models. The conductive and resistive blocks of the checkerboard patterns were more clearly recovered by using the measurement configuration of the geomagnetic data (Figures 7a′ and 7b′) than when using the configuration of the Network-MT data (Figures 7a″ and 7b″), with the exception of Aso's peripheral regions (blue outline in Figures 7a′ and 7b′), which show no/few geomagnetic observation sites (also see Figures 1b and 2a).

Figures $7a'_{mr}$–$7d'_{mr}$ and $7a''_{mr}$–$7d''_{mr}$ show "model recovery" images [*Zhang et al*., 2012], which indicate differences between the original checkerboard pattern model $\mathbf{m_{true}}$ (Figures 7a–7d), and the resolution test model (the synthetic model) $\mathbf{m_{model}}$ (Figures 7a′–7d′ and 7a″–7d″). The model recovery is defined as

$$\delta\mathbf{m} = log(\mathbf{m_{model}}/\mathbf{m_{true}}) = log(\mathbf{m_{model}}) - log(\mathbf{m_{true}}).$$

Colorless blocks indicate good recovery, whereas deep-colored blocks indicate weak recovery. Deep red and blue blocks are originally preferable to become more conductive and resistive. For quantitative verification, we determined the RMS of the model recovery, $\mathrm{RMS}(\mathbf{m}) = \sqrt{\sum_{i=1}^{M_{free}} \delta m_i^2 / M_{\mathrm{free}}}$, as defined by *Zhang et al*. [2012], where M_{free} is the model parameter size (110,683 cells), except for in seawater blocks, which are fixed at 0.33 Ωm. The model recovery, RMS(**m**), is 0.5794 for Figure $7a'_{mr}$, 0.5728 for Figure $7b'_{mr}$, 0.4726 for Figure $7c'_{mr}$, 0.4745 for Figure $7d'_{mr}$, 0.5809 for Figure $7a''_{mr}$, 0.5839 for Figure $7b''_{mr}$, 0.4741 for Figure $7c''_{mr}$, and 0.4719 for Figure $7d''_{mr}$. The RMS(**m**) values for the measurement configuration of the geomagnetic data (Figures $7a'_{mr}$–$7c'_{mr}$), excluding (Figure $7d'_{mr}$), are less than the RMS(**m**) values for the configuration of the Network-MT data (Figures $7a''_{mr}$–$7c''_{mr}$), in corresponding models.

Model recovery images indicate that at shallow depths the configuration of the geomagnetic data (Figures $7a'_{mr}$ and $7b'_{mr}$) has a resolution higher than the configuration of the Network-MT data (Figures $7a''_{mr}$ and $7b''_{mr}$), based on the block size (25 × 25 × 10 km). For the checkerboard patterns of larger blocks (Figures 7c′ and 7d′), conductive blocks with dense geomagnetic observation sites are clearly recovered, even though the conductive blocks seem to spread to other conductive blocks in areas of sparse

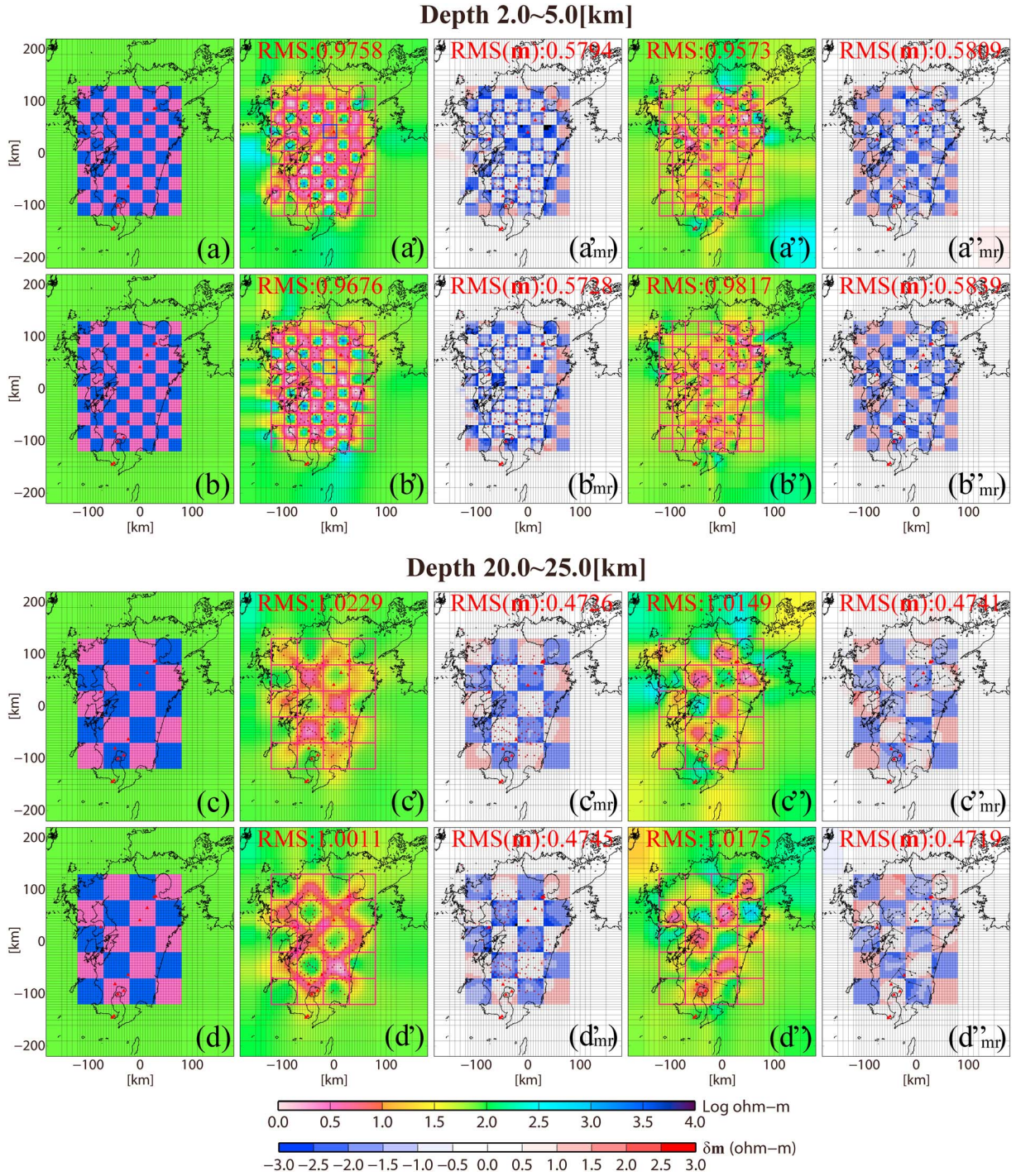

Figure 7. (a–d) Plan views of four checkerboard patterns used in resolution tests in this study, and (a′–d′) views of eight resolution test models obtained using (a″–d″) the actual measurement configuration provided by the 136 geomagnetic TFs obtained using the configuration of the 72 Network-MT RFs. The other eight plan views (Figures 7a′$_{mr}$–7d′$_{mr}$ and 7a″$_{mr}$–7d″$_{mr}$) are images of model recovery for the eight resolution test models. The four checkerboards (Figures 7a–7d) were used to obtain the synthetic data to which 5% Gaussian noise was added before the inversion. Patterns in Figures 7a and 7c are opposite those of Figures 7b and 7d, respectively. The resistivity values of the conductive and resistive blocks in all checkerboard patterns are 3 Ωm and 3000 Ωm, respectively. All checkerboard patterns have dimensions of 250 × 200 km in the *X* and *Y* directions. The patterns of Figures 7a and 7b and those of Figures 7c and 7d consist of 80 blocks (25 × 25 km alternately in the horizontal direction) and 20 blocks (50 × 50 km alternately in the horizontal direction), respectively. The thicknesses of inserted checkerboard patterns are set to 0–10 km (Figures 7a and 7b) and 10–40 km (Figures 7c and 7d) in the vertical direction. Eight plan view sections (Figures 7a′–7d′ and 7a″–7d″), of the inverted models show sections 2–5 km in depth (Figures 7a′ and 7b′ and 7a″ and 7b″) and 20–25 km in depth (Figures 7c′ and 7d′ and 7c″ and 7d″). Volcanoes (red triangles) are shown in each section, while the 136 geomagnetic observation sites (red dots) are shown in the four sections (Figures 7a′–7d′), and the 72 dipoles (black lines with endpoints) are shown in the other four sections (Figures 7a″–7d″).

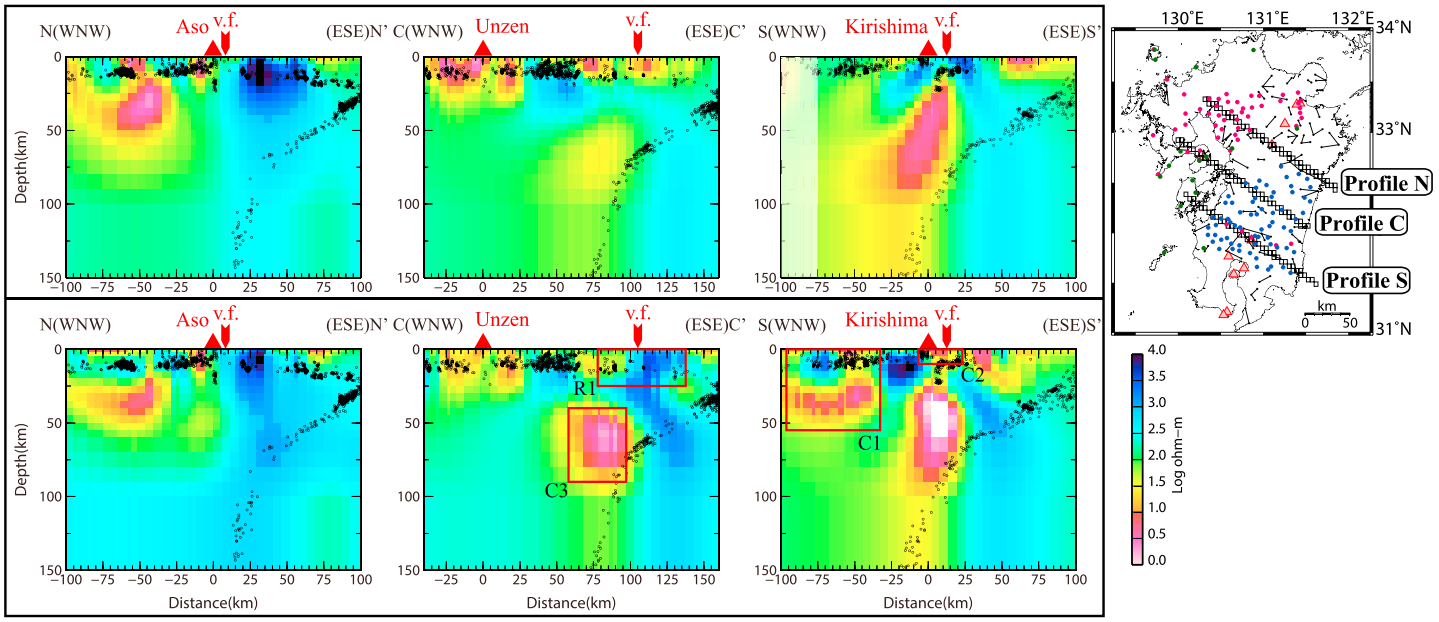

Figure 8. Comparison between cross sections of the two final 3-D resistivity models along the three profiles shown on the inset map (top right). Selected meshes along the three profiles, the 136 geomagnetic observation sites (red, blue, and green dots), the 72 Network-MT dipoles (black lines with endpoints), and active volcanoes (red triangles) are shown together on the map. The three cross sections in the top row and those in the top row show the final 3-D model obtained using the Network-MT RFs from *Hata et al.* [2015] and the final 3-D model obtained using the 136 geomagnetic TFs in this study, respectively. The black dots on the cross sections are the hypocenters of earthquakes within 10 km of each profile, as determined by the JMA from June 2002 to May 2006. The red arrows labeled v.f. represent the position of the volcanic front. In the final 3-D model along profiles S and C of the lower row, three conductive regions (C1, C2, and C3) and a resistive region (R1), which are marked with four red boxes, are examined to test the model sensitivity.

observation sites, across the boundaries of the respective blocks, especially as shown in Figure 7d′. The spreading conductive blocks are probably due to the nature of the geomagnetic TFs, which have a tendency to connect conductive blocks horizontally, because the geomagnetic TFs are sensitive to horizontal variations in the electrical resistivity structure. Besides the recovery for the conductive blocks, that of the resistive blocks in all configurations of the geomagnetic and the Network-MT data are imperfect. However, as a whole, the block sizes of conductive anomalies, which are represented in the resolution test models using the configuration of the geomagnetic data (Figures 7a′–7d′), are potentially resolvable in both horizontal and vertical directions over land areas. Moreover, our previous 3-D resistivity model can be improved by introducing the geomagnetic TF data.

5. Results and Discussion

Results of the final 3-D resistivity model are summarized in the three cross sections in the lower row of Figure 8 and in the horizontal cross sections in Figure 9 (plan view and perspective view in the top and bottom rows, respectively). The cross sections in Figure 8 are approximately parallel to the horizontal movement direction of the subducting PSP (N60°W–S60°E) beneath Kyushu. Two profiles, S and N in Figure 8, traverse the Kirishima and Aso volcanoes on the volcanic front in the two volcanic regions. Profile C, which passes over Unzen volcano in the back arc , crosses the nonvolcanic region in central Kyushu, as shown in Figure 1. In addition, profile S crosses the Kagoshima Graben (KG) and profiles N and C cross the BSG. The horizontal cross sections in Figure 9 are constructed at depths of 2–5, 20–25, and 45–50 km.

In large scale, the final 3-D resistivity model of the present study, in the bottom row of Figure 8, shows common features with the initial large-scale 3-D resistivity model [*Hata et al.*, 2015]. One of these features is the spatial relationship between conductive blocks extending from the mantle (>40 km in depth) and the subducting PSP imaged by hypocenters, on the three cross sections in the lower row of Figure 8. The conductive blocks, which are located to the northwest of Aso volcano in the northern volcanic region on profile N, exist at some distance from the subducting PSP, at depths of <100 km. Another conductive block (C3) located beneath the nonvolcanic region on profile C occurs along the subducting PSP, from greater depths of

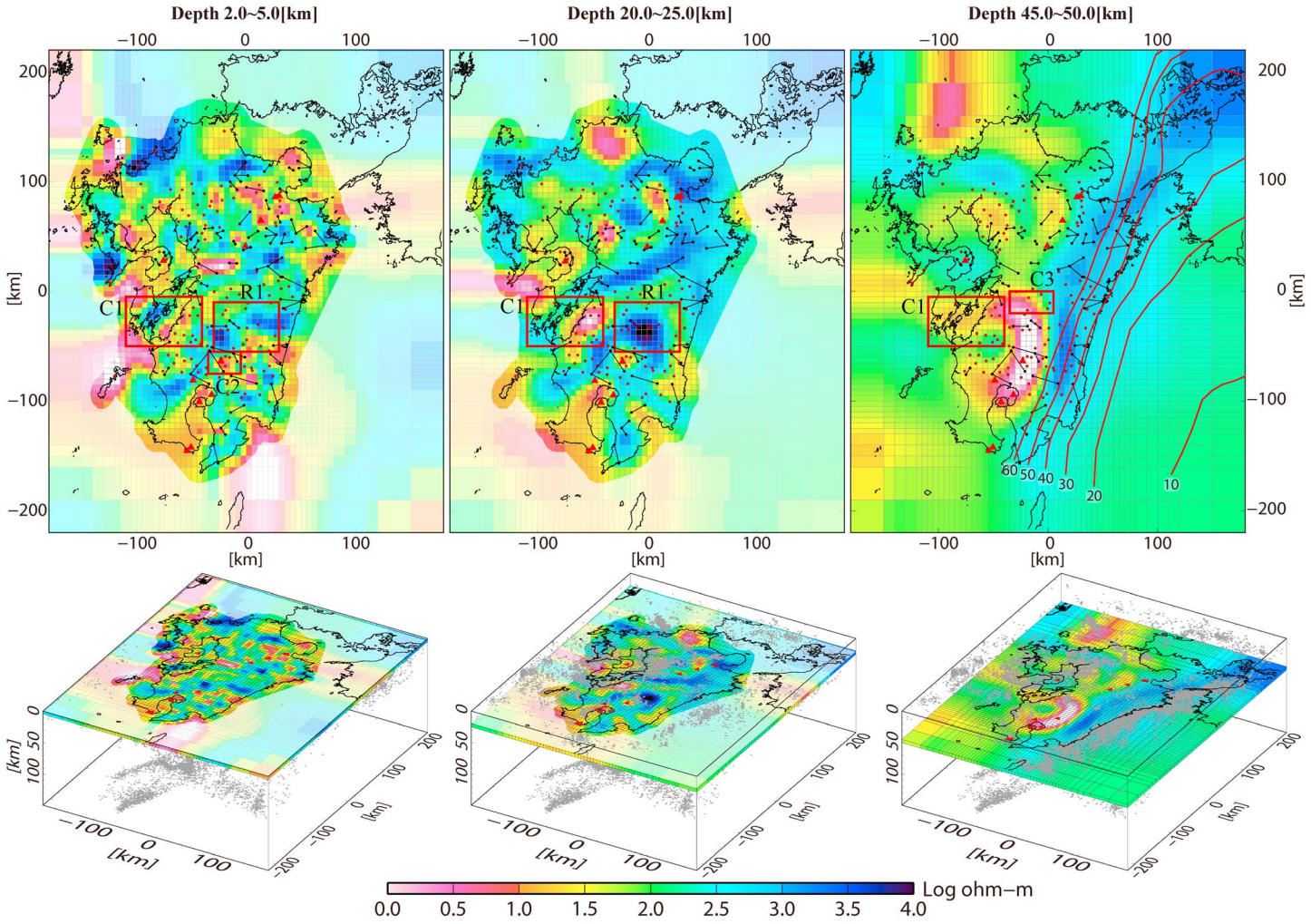

Figure 9. Horizontal cross sections of the final 3-D resistivity model at depths of 2–5, 20–25, and 45–50 km. Three conductive regions (C1, C2, and C3) and a resistive region (R1), which are marked with four red boxes, are examined to test the model sensitivity. The red dots and black lines with endpoints on the three sections on the upper row are the 136 geomagnetic observation sites and the 72 Network-MT dipoles, respectively. The red solid curved lines on the cross section at depths of 45–50 km are isodepth contours of the upper surface of the subducting PSP (10–60 km), estimated from the results of *Baba et al.* [2002], *Nakajima and Hasegawa* [2007], and *Hirose et al.* [2008]. The gray dots on the three sections on the lower row are the hypocenters of earthquakes, as determined by the JMA from June 2002 to May 2006. The red triangles represent active Quaternary volcanoes.

~100 km to a depth of ~50 km. A conductive block located beneath Kirishima volcano in the southern volcanic region on profile S occurs along the subducting PSP from depths of >100 km and extends into the crust. The conductive blocks with different spreads and structures in the three regions are regarded as upwelling fluids (aqueous fluids and/or partial melts); details of such structures are discussed by *Hata et al.* [2015]. The other common feature on the three profiles is each resistive block on the fore-arc side, including the descending slab, as compared with blocks on the back-arc side. This feature can be clearly observed on the horizontal cross section at a depth of 45–50 km, as shown in Figure 9.

On the other hand, the presence of small-scale features at depths of < ~50 km (R1 on profile C and C1 and C2 on profile S; see Figure 8) is a significant departure from the results of the previous model for profiles C and S; notably, the geomagnetic observation sites are densely distributed along these profiles. Thus, we performed the following three tests to determine whether the sensitivity of our inversion modeling is sufficient to resolve the three anomalies through 3-D forward modeling. In one of the three sensitivity tests, cells in the block with resistivity values of >80 Ωm (feature R1, at depths of 0–25 km, with a north-south length of 40 km and an east-west width of 60 km), located beneath the nonvolcanic region, were replaced by cells with resistivity values of 80 Ωm. In another sensitivity test, cells with values of <80 Ωm in the conductive block (feature C1, at depths

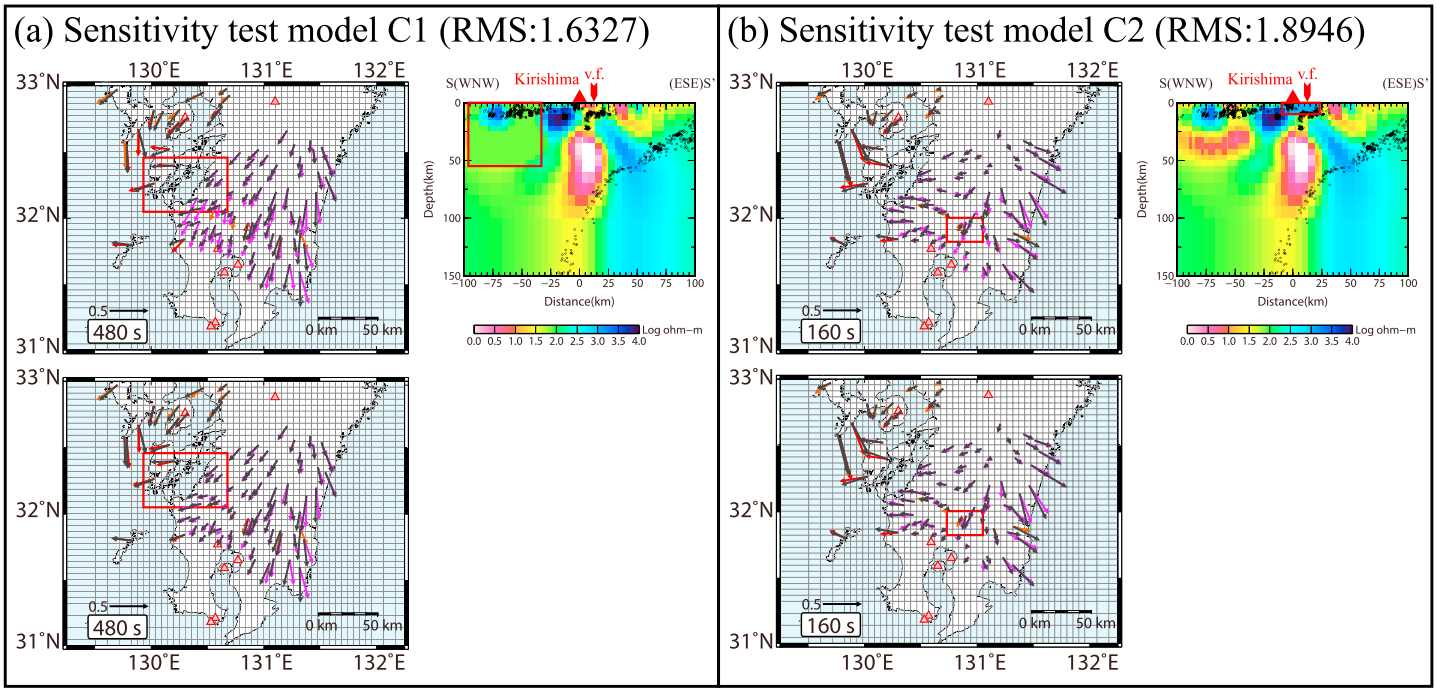

Figure 10. Sensitivity test models and results for the final 3-D model along Profile S. Two conductive regions, (a) C1 and (b) C2, are replaced by relatively resistive blocks to examine the sensitivity of the model. The observed induction arrows (gray arrows) and synthetic induction arrows (colored arrows) are indicated on respective maps, at periods of 480 s or 160 s, for real parts of the geomagnetic TFs. The colored arrows on the upper maps and those on the lower maps are obtained from each sensitivity test model and the final model. All other symbols in the figure are the same as in previous figures.

of 0–55 km, with a length of 45 km and a width of 70 km), located on the back-arc side of Kirishima volcano, were replaced by cells with values of 80 Ωm. In the other sensitivity test, cells with values of $<$1000 Ωm in the second conductive block (feature C2, at depths of 0–10 km, with a length of 20 km and a width of 30 km), located beneath Kirishima volcano, were replaced by cells with resistivities of 1000 Ωm. Figures 10a, 10b, and 12b present respective cross sections along profiles S and C, showing the three sensitivity test models. Significant changes in the geomagnetic TFs are determined and found in synthetic induction arrows especially in and around the replaced blocks/regions on the maps in Figures 10 and 12. The synthetic induction arrows tend to depart from the observed arrows. In addition, RMS misfits for the sensitivity test models (1.6327 for C1, 1.8946 for C2, and 1.5742 for R1) are significantly increased as compared with the RMS misfit for the final model of 0.9981. Thus, the three anomalies are considered to be significant features.

We consider that the conductive anomaly in feature C1 (see the cross section on profile S; Figure 8), which was newly detected in this study, indicates the presence of hydrothermal fluids and hydrothermal alteration zones associated with the epithermal gold deposits in the Hisatsu and Hokusatsu zones, as shown in Figure 1b. A similar conductive anomaly, above which epithermal gold deposits distribute on the west side of the Hohi volcanic zone, was detected beneath the western end of profile N at depths of $<$ ~50 km. Thus, the two anomalies are considered to be a common structure associated with the epithermal gold deposits. The newly detected anomaly, C1, can also be regarded as a crucial factor in explaining the westward pointing induction arrows on the west coast of southern Kyushu (see the induction arrows in Figure 10a). The induction arrows from the final model show a good fit to the observed arrows, which remained unexplained in previous model calculations based on either the thin sheet analysis or the 2-D inversion analysis [e.g., *Shimoizumi et al*., 1997; *Handa*, 2005]. Our model indicates that the westward induction arrows result from the conductive anomaly at shallow depths of ~50 km/at the crust in the vicinity of Kyushu, whereas the previous model calculations mainly tried to explain the westward arrows by a conductive anomaly, which is associated with the Okinawa trough in Figure 1, at deep depths/at the mantle beneath the East China Sea distant from the land. Furthermore, the conductive anomaly C1 locates on an extension line of a seismic belt, including a magnitude 7.3 main shock (at a depth of 12 km, 15 April 2016 at 16:25 UTC) and a magnitude 6.5 foreshock (at a depth of

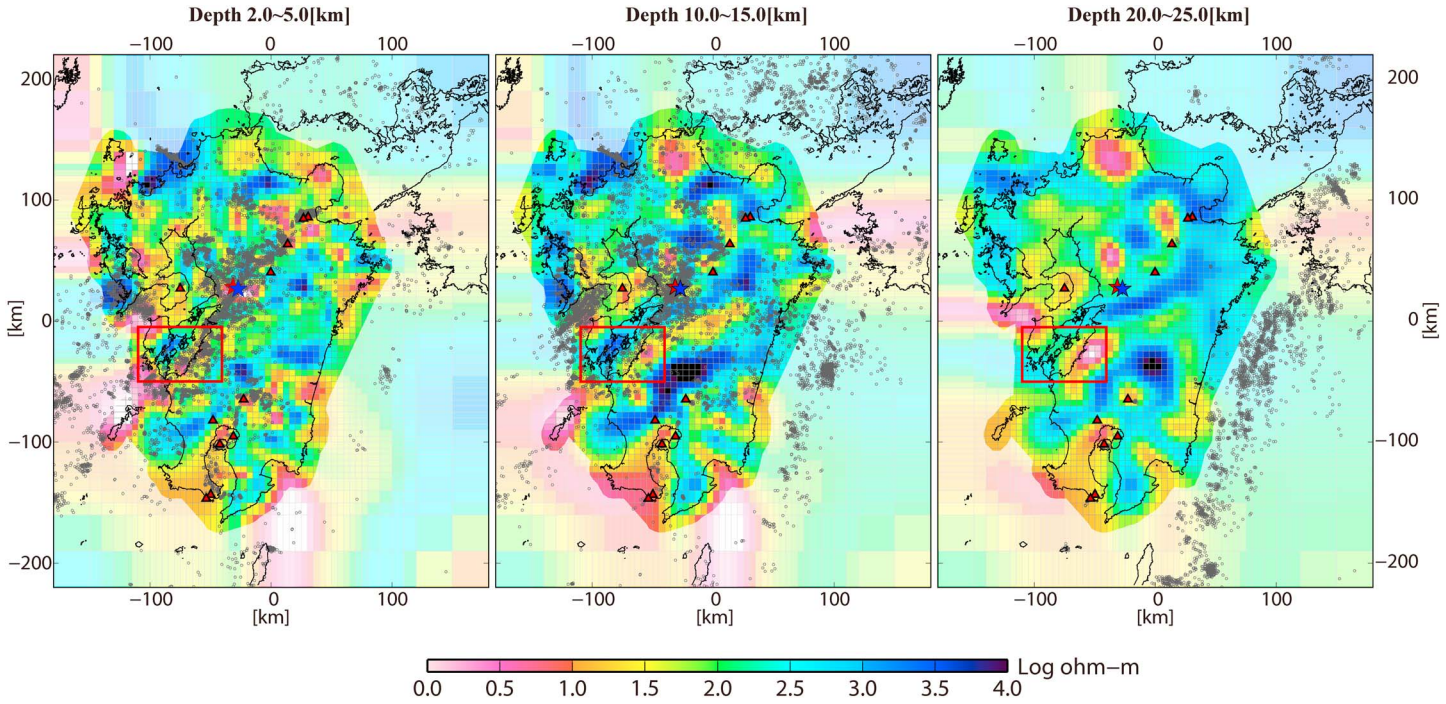

Figure 11. Horizontal cross sections of the final 3-D resistivity model at depths of 2–5, 10–15, and 20–25 km with the hypocenters of earthquakes (gray dots) determined by the JMA from January 2014 to April 2016. The red and blue stars denote a magnitude 7.3 main shock (at a depth of 12 km, 15 April 2016 at 16:25 UTC) and a magnitude 6.5 foreshock (at a depth of 11 km, 14 April 2016 at 12:26 UTC) of the 2016 Kumamoto earthquakes. The red triangles represent active Quaternary volcanoes. A red box represents the conductive anomaly C1, which is replaced region for the sensitivity test.

11 km, 14 April 2016 at 12:26 UTC) of the 2016 Kumamoto earthquakes, along the BSG as shown on a horizontal cross section at a depth of 10–15 km in Figure 11. At the depth, the earthquakes distribute in relatively resistive areas. On the other hand, the earthquakes are found to almost continuously distribute in both resistive and conductive areas on a horizontal cross section at a depth of 2–5 km in Figure 11.

Feature C2, the other conductive anomaly (see the cross section along profile S; Figure 8), which is located in the crust beneath Kirishima volcano in the southern volcanic region, forms part of a continuous conductive block from the mantle to the ground surface. The feature is considered to represent upwelling fluids composed of slab-derived aqueous fluids and partial melts. We thus succeeded in clearly capturing the upwelling fluids in this study. *Miyoshi et al*. [2010], based on a geochemical investigation, report that the source-mantle compositions of the Kirishima basalts are highly influenced by modern slab-derived fluids compared with those of the basalts from the other volcanoes on Kyushu. The resistive anomaly of feature R1 (located on the cross section on profile C; Figure 8), which was also newly detected in this study, occurs in the crust beneath the nonvolcanic region. The feature that is required by the data is considered to be real, considering that no active volcanoes are present in the region. We therefore conclude that upwelling fluids in the mantle beneath the nonvolcanic region have failed to break through the crust because the addition of slab-derived aqueous fluids to the mantle beneath the region is too small to accelerate partial melting of the mantle [*Hata et al*., 2015].

We performed another sensitivity test for a conductive block, located in C3 on the cross section of profile C, through 3-D forward modeling, to examine whether the conductive block with resistivity values of $<40\,\Omega$m is necessary for the final 3-D model (see Figure 8). This sensitivity test was strongly related to the discussion above on upwelling fluids beneath the nonvolcanic region. In the sensitivity test, cells with values of $<40\,\Omega$m in the conductive block (feature C3, at depths of 40–90 km and with a north-south length of 20 km and an east-west width of 40 km) beneath the nonvolcanic region were replaced by cells with values of $40\,\Omega$m, as shown in Figure 12a. Figure 12a also shows a cross section along profile C of the sensitivity test model. We found no essential changes between the synthetic induction arrows of the sensitivity test model and those for the final model in and around the replaced blocks/regions on the maps in Figure 12a. The RMS misfit of 1.0001 for the sensitivity test model is only 0.002 greater than the RMS misfit of 0.9981 for the final

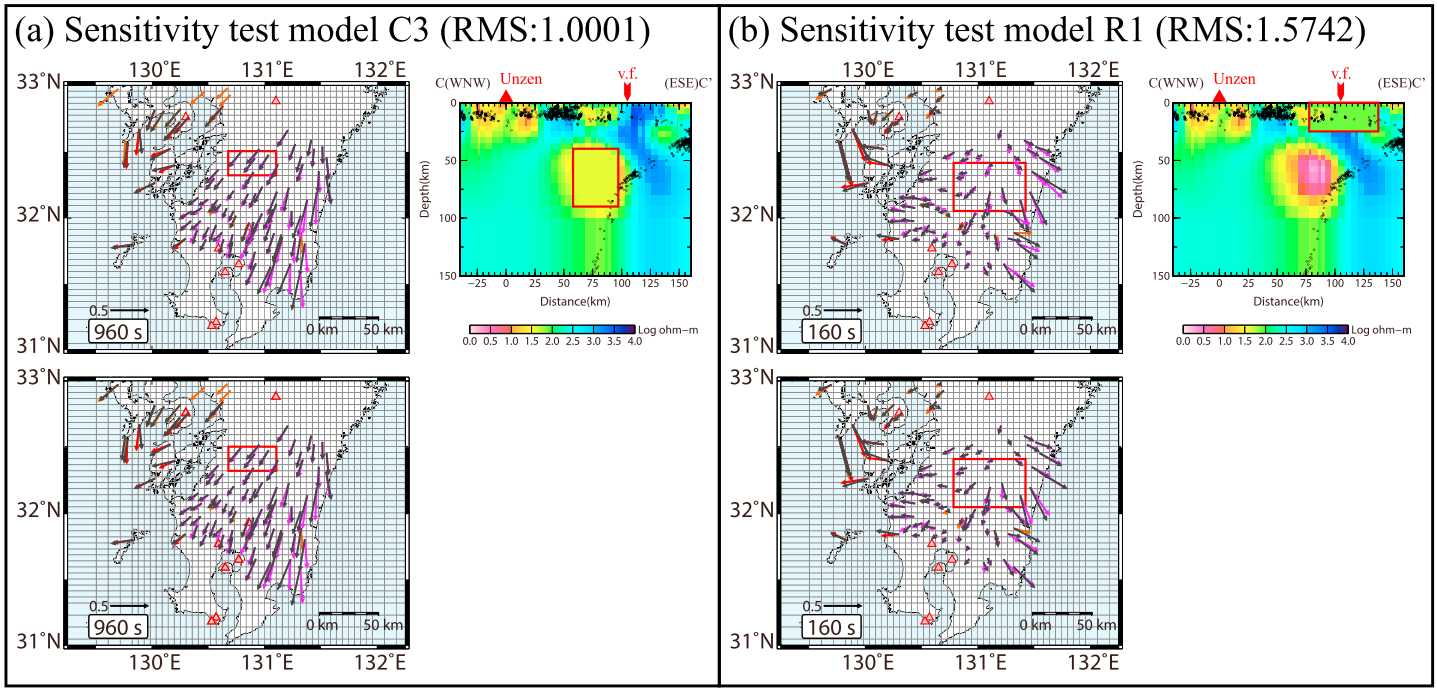

Figure 12. Sensitivity test models and results of the final 3-D model along Profile C. (a) A conductive region, C3, and (b) a resistive region, R1, are replaced with a relatively resistive block and a relatively conductive block, respectively, to examine the sensitivity of the model. Observed induction arrows (gray arrows) and synthetic induction arrows (colored arrows) are shown on respective maps, at periods of 960 s or 160 s, for real parts of the geomagnetic TFs. The colored arrows on the upper maps and those on the lower maps are obtained from each sensitivity test model and the final model. All other symbols in the figure are the same as in previous figures.

model. This result indicates that values of $<40\,\Omega$m, which are expressed as a notable conductive anomaly in the final model (see the cross section of profile C in the lower row of Figure 8), and the value of 40 Ωm, which is expressed as a relatively conductive anomaly in the initial 3-D model of *Hata et al.* [2015] (top row of Figure 8), are both acceptable. We consider that a certain amount of slab-derived aqueous fluid is released from the subducting PSP beneath the nonvolcanic region (although the quantity of these fluids would be less than the amount beneath the southern volcanic region) and that the fluids are detected as a (relatively) conductive anomaly in the 3-D resistivity models. This relatively small amount of slab-derived aqueous fluid does not result in the partial melting of mantle required to accelerate arc magmatism/volcanism beneath the nonvolcanic region, and the upwelling fluids in the mantle fail to break through the crust. This finding also reinforces an argument inferred from the previous 3-D model in *Hata et al.* [2015].

We compared the significant resistive feature on the fore-arc side, which widely extends along the coastline, with the isodepth contours of the upper surface of the subducting PSP (10–60 km), as estimated from the results of marine seismic refraction surveys by *Baba et al.* [2002] and seismic tomography imaging by *Nakajima and Hasegawa* [2007] and *Hirose et al.* [2008]. The isodepth contours of the upper surface of the subducting PSP are shown on the horizontal cross-section at a depth of 45–50 km in Figure 9. The cross section represents the resistivity structure at the upper mantle, because the continental Moho beneath Kyushu is expected to be at a depth of <40 km based on receiver function analysis [*Abe et al.*, 2013]. The resistive block/anomaly at the depth of 45–50 km (in Figure 9), which extends more closely to the east face of the volcanoes than do the isodepth contours of 40–50 km, bends in the nonvolcanic region. Moreover, the resistive anomaly does not extend in parallel with the isodepth contours. The extent and shape of the resistive anomaly are considered to be attributed to the subducting PSP consisting of the three parts (a younger region underlying the Shikoku Basin, an older portion, and a part of the Kyushu–Palau Ridge) in Figure 1a. The resistivity values of the mantle are dependent on several factors such as mantle minerals, the presence of fluids (aqueous fluids and/or melts), and temperature [e.g., *Hata and Uyeshima*, 2015]. Thus, the resistive anomaly in the fore arc is considered to be controlled by the interaction between the subducting cold PSP consisting of the three parts and the overlying hot mantle.

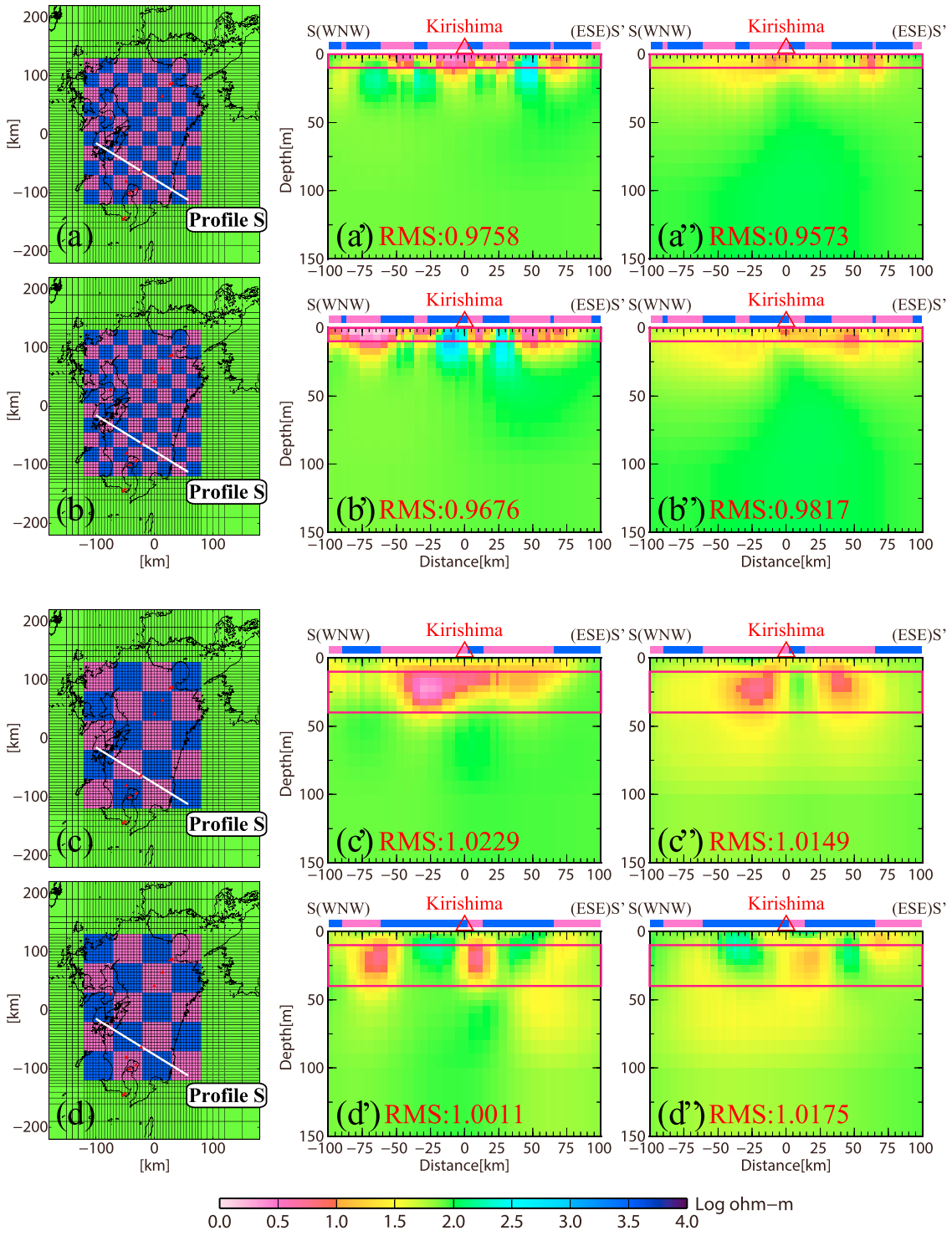

Figure A1. (a–d) Plan views of four checkerboard patterns used in resolution tests in this study, and (a′–d′) cross sections along profile S of eight resolution test models obtained by using (a″–d″) the actual measurement configuration provided by the 136 geomagnetic TFs obtained using the configuration of the 72 Network-MT RFs. The four checkerboards (Figures A1a–A1d) were used to obtain the synthetic data, to which 5% Gaussian noise was added before the inversion. Patterns in Figures A1a and A1c are opposite those of Figures A1b and A1d, respectively. The resistivity values of the conductive and resistive blocks in all checkerboard patterns are 3 Ωm and 3000 Ωm, respectively. All checkerboard patterns have dimensions of 250 × 200 km in the *X* and *Y* directions. The patterns of Figures A1a and A1b and those of Figures A1c and A1d consist of 80 blocks (25 × 25 km alternately in the horizontal direction) and 20 blocks (50 × 50 km alternately in the horizontal direction), respectively. The thicknesses of inserted checkerboard patterns are set to 0–10 km (Figures A1a and A1b) and 10–40 km (Figures A1c and A1d) in the vertical direction, which are represented with red boxes on the cross sections. Respective checkerboard patterns along the profile are expressed by bars over the cross sections. The red triangles represent Kirishima volcano.

6. Conclusions

The well-determined electrical resistivity model beneath the island of Kyushu, based on a previous large-scale model [*Hata et al*., 2015], was obtained through a 3-D inversion analysis by introducing geomagnetic TFs as additional input data. As expected from the resolution tests, the final 3-D model using the actual measurement configuration of the geomagnetic data shows higher resolutions, especially for small-scale structures at shallow depths, than the previous model. This result shows improved resolution at crustal depth using different data sets, without any joint inversion.

The vertical cross sections in the final 3-D model, which intersect the northern and southern volcanic regions and the nonvolcanic region on Kyushu, newly reveal the following three features. The first feature is conductive block C1, located on the back-arc side of Kirishima volcano at shallow depths of ~50 km. The conductive block is considered to be associated with hydrothermal fluids and hydrothermal alteration zones that formed the epithermal gold deposits in the Hisatsu and Hokusatsu zones. The second feature is conductive block C2, located in the crust beneath Kirishima volcano in the southern volcanic region. The conductive block forms part of a clear anomaly, which is regarded as upwelling fluids, from the mantle to the ground surface. The third feature is resistive block R1, located in the shallow crust beneath the nonvolcanic region (in contrast to conductive block C3, which exists in the mantle); R1 is considered to be associated with the nonvolcanic region.

The horizontal cross sections in the final 3-D model show a marked resistive anomaly beneath the continental Moho on the fore-arc (eastern) side of the volcanic front. The resistive anomaly is horizontally distributed and connects the east faces of respective volcanoes in the northern and southern volcanic regions, and bends in the central nonvolcanic region. It suggests that the resistive anomaly is associated with the magmatism/volcanism beneath the three regions, the one nonvolcanic and two volcanic regions, in Kyushu. The distribution of the anomaly is considered to be produced by the interaction between the three parts of the subducting cold PSP and the overlying hot mantle.

Acknowledgments

We express our gratitude to N. Oshiman, R. Yoshimura, and T. Uchide for initial discussions related to this study. We thank W. Siripunvaraporn and coworkers for providing the WSINV3DMT code. We also thank A.D Chave and D.J. Thomson for providing their robust remote-reference magnetotelluric (BIRRP) code. We appreciate two anonymous reviewers for their useful comments which helped to improve the manuscript. The figures were created using Generic Mapping Tools [*Wessel and Smith*, 1998]. We used hypocenter data from the JMA Unified Earthquake Catalog. We used the computer systems of the Earthquake Information Center of the Earthquake Research Institute, University of Tokyo. This research was partially supported by JSPS KAKENHI grants and grants offered under the Earthquake and Volcanic Eruption Prediction Research programs from the Ministry of Education, Culture, Sports, Science and Technology. All data are available for evaluating the contents of this paper; the data can be requested by contacting M.H. (m.hata@aist.go.jp). For the other uses, the availability of the data will be determined on a case-by-case basis by M.U. (uyeshima@eri.u-tokyo.ac.jp) because the data cannot be released to the public.

References

Abe, Y., T. Ohkura, K. Hirahara, and T. Shibutani (2013), Along-arc variation in water distribution in the uppermost mantle beneath Kyushu, Japan, as derived from receiver function analyses, *J. Geophys. Res. Solid Earth*, *118*, 3540–3556, doi:10.1002/jgrb.50257.

Baba, T., Y. Tanioka, P. R. Cummins, and K. Uhira (2002), The slip distribution of the 1946 Nankai earthquake estimated from tsunami inversion using a new plate model, *Phys. Earth Planet. Inter.*, *132*, 59–73.

Chave, A. D., and D. J. Thomson (1989), Some comments on magnetotelluric response function estimation, *J. Geophys. Res.*, *94*, 14,215–14,225, doi:10.1029/JB094iB10p14215.

Chave, A. D., and D. J. Thomson (2004), Bounded influence magnetotelluric response function estimation, *Geophys. J. Int.*, *157*, 988–1006.

Chave, A. D., D. J. Thomson, and M. E. Ander (1987), On the robust estimation of power spectra, coherences, and transfer functions, *J. Geophys. Res.*, *92*, 633–648, doi:10.1029/JB092iB01p00633.

Egbert, G. D., J. R. Booker, and A. Schultz (1992), Very long period magnetotelluric at Tucson Observatory: Estimation of impedance, *J. Geophys. Res.*, *97*, 15,113–15,128, doi:10.1029/92JB01252.

Fujii, I. (2004), Method to estimate geomagnetic total intensity variations due to volcanic activities by using the stochastic differential method [in Japanese with English abstract], *Tech. Rep. Kakioka Magn. Obs.*, *2*(1), 1–15.

Fujiwara, S., and H. Toh (1996), Geomagnetic transfer functions in Japan obtained by first order geomagnetic survey, *J. Geomag. Geoelectr.*, *48*, 1071–1101.

Handa, S. (2005), Electrical conductivity structures estimated by thin sheet inversion, with special attention to the Beppu-Shimabara graben in central Kyushu, Japan, *Earth Planets Space*, *57*, 605–612.

Handa, S., Y. Tanaka, and A. Suzuki (1992), The electrical high conductivity layer beneath the northern Okinawa Trough, inferred from geomagnetic depth sounding in Northern and Central Kyushu, Japan, *J. Geomag. Geoelectr.*, *44*, 505–520.

Hata, M., and M. Uyeshima (2015), Temperature and melt fraction distributions in a mantle wedge determined from the electrical conductivity structure: Application to one nonvolcanic and two volcanic regions in the Kyushu subduction zone, Japan, *Geophys. Res. Lett.*, *42*, doi:10.1002/2015GL063308.

Hata, M., N. Oshiman, R. Yoshimura, Y. Tanaka, and M. Uyeshima (2012), Fluid upwelling beneath arc volcanoes above the subducting Philippine Sea Plate: Evidence from regional electrical resistivity structure, *J. Geophys. Res.*, *117*, B07203, doi:10.1029/2011JB009109.

Hata, M., N. Oshiman, R. Yoshimura, Y. Tanaka, and M. Uyeshima (2015), Three-dimensional electromagnetic imaging of upwelling fluids in the Kyushu subduction zone, Japan, *J. Geophys. Res. Solid Earth*, *120*, 1–17, doi:10.1002/2014JB011336.

Hayasaka, S. (1987), Geologic structure of Kagoshima Bay, South Kyushu, Japan [in Japanese with English abstract], *Mono. Assoc. Geol. Collab.*, *33*, 225–233.

Hirose, F., J. Nakajima, and A. Hasegawa (2008), Three-dimensional seismic velocity structure and configuration of the Philippine Sea slab in southwestern Japan estimated by double-difference tomography, *J. Geophys. Res.*, *113*, B09315, doi:10.1029/2007JB005274.

Kamata, H. (1989), Volcanic and structural history of the Hohi volcanic zone, central Kyushu, Japan, *Bull. Volcanol.*, *51*, 315–332.

Matsui, K., T. Furukawa, and K. Sawamura (1989), Geology of the Sasebo district, Geological Map at 50,000 [in Japanese with English abstract], *Geol. Surv. Japan*, 92 pp.

Matsumoto, Y. (1979), Some problems on volcanic activities and depression structures in Kyushu, Japan [in Japanese with English abstract], *Mem. Geol. Soc. Jpn.*, *16*, 127–139.

Miyoshi, M., M. Shimono, T. Hasenaka, T. Sano, Y. Mori, and T. Fukuoka (2010), Boron systematics of Hisatsu and Kirishima basaltic rocks from southern Kyushu, Japan, *Geochem. J.*, *44*, 359–369.

Munekane, H. (2000), Correction of the galvanic effect in magnetotellurics and its application to regional sounding of Southern Kyushu Area, PhD thesis, the University of Tokyo, Japan.

Munekane, H., et al. (1997), Resistivity survey across the southern part of the Kyushu Island [in Japanese with English abstract], *Bull. Earthq. Res. Inst. Univ. Tokyo*, *72*, 19–65.

Nagao, T., Y. Hase, S. Nagamine, S. Kakubuchi, and K. Sakaguchi (1999), Late Miocene to middle Pleistocene Hisatsu volcanic rocks generated from heterogeneous magma sources: Evidence from temporal-spatial variation of distribution and chemistry of the rocks [in Japanese with English abstract], *J. Miner. Petrol. Econ. Geol.*, *94*, 461–481.

Nakajima, J., and A. Hasegawa (2007), Subduction of the Philippine Sea Plate beneath southwestern Japan: Slab geometry and its relationship to arc magmatism, *J. Geophys. Res.*, *112*, B08306, doi:10.1029/2007JD009009.

Parkinson, W. D. (1962), The influence of continents and oceans on geomagnetic variations, *Geophys. J. Int.*, *6*, 441–449.

Rikitake, T. (1969), The undulation of an electrically conductive layer beneath the islands of Japan, *Tectonophysics*, *7*, 257–264.

Rikitake, T., and I. Yokoyama (1953), Anomalous relations between H and Z components of transient geomagnetic variations, *J. Geomag. Geoelectr.*, *5*, 59–65.

Shimoizumi, M., T. Mogi, M. Nakada, T. Yukutake, S. Handa, Y. Tanaka, and H. Utada (1997), Electrical conductivity anomalies beneath the western sea of Kyushu, Japan, *Geophys. Res. Lett.*, *24*, 1551–1554, doi:10.1029/97GL01542.

Siripunvaraporn, W., and G. Egbert (2009), WSINV3DMT: Vertical magnetic field transfer function inversion and parallel implementation, *Phys. Earth Planet. Inter.*, *173*(3–4), 317–329.

Siripunvaraporn, W., M. Uyeshima, and G. Egbert (2004), Three-dimensional inversion for Network-Magnetotelluric data, *Earth Planets Space*, *56*, 893–902.

Toh, H., and S. Honma (2008), Mantle upwelling revealed by genetic algorithm inversion of the magnetovariational anomaly around Kyushu island, Japan, *J. Geophys. Res.*, *113*, B10103, doi:10.1029/2006JB004891.

Uyeshima, M. (2007), EM monitoring of crustal processes including the use of the Network-MT observations, *Surv. Geophys.*, *28*, 199–237.

Wessel, P., and W. H. F. Smith (1998), New, improved version of generic mapping tools released, *Eos Trans. AGU*, *79*, 579, doi:10.1029/98EO00426.

Yukutake, T., J. H. Filloux, J. Segawa, Y. Hamano, and H. Utada (1983), Preliminary report on a magnetotelluric array study in the Norhtwest Pacific, *J. Geomag. Geoelectr.*, *35*, 575–587.

Zhang, L., T. Koyama, H. Utada, P. Yu, and J. Wang (2012), A regularized three-dimensional magnetotelluric inversion with a minimum gradient support constraint, *Geophys. J. Int.*, *189*, 296–316.